Contents lists available at ScienceDirect

Arabian Journal of Chemistry

journal homepage: www.ksu.edu.sa

Original article

Remarkable CO_2 photocatalytic reduction enabled by UiO-66-NH_2 anchored on flower-like $ZnIn_2S_4$

Huimin Yu, Shaohong Guo *, Meilin Jia, Jingchun Jia, Ying Chang, Jiang Wang

College of Chemistry and Environmental Science, Inner Mongolia Key Laboratory of Green Catalysis and Inner Mongolia Collaborative Innovation Center for Water Environment Safety, Inner Mongolia Normal University, Hohhot 010022, China

ABSTRACT

The utilization of renewable solar energy for the photocatalytic transformation of carbon dioxide (CO_2) into valuable chemical substances is considered an optimal strategy to simultaneously address climate challenges and tackle energy scarcity. Herein, we prepared heterojunction photocatalysts UiO-66-NH_2/$ZnIn_2S_4$, which were successfully applied in the photocatalytic reduction of CO_2. The yield of the main product CO, for the optimal UiO-66-NH_2/$ZnIn_2S_4$-2 sample could reach up to 57 μmol $g^{-1}h^{-1}$ when converting CO_2 under the visible light irradiation, which was approximately 3.35 and 2.71 times higher than that achieved by the individual UiO-66-NH_2 and $ZnIn_2S_4$ samples, respectively. The better photocatalytic performance of the UiO-66-NH_2/$ZnIn_2S_4$-2 composites can be attributed to its synergistic effect resulting from tight interfacial contacts, special charge transfer pathways and excellent CO_2 adsorption capacity. Furthermore, the intimate contact between UiO-66-NH_2 and flower-like $ZnIn_2S_4$ accelerates electron transmission while effectively suppressing the quenching of photogenerated carriers. This research provides vital knowledge for the rational design of heterostructures aimed at enhancing the efficiency of CO_2 photocatalysis for solar fuel production.

1. Introduction

The pressing global energy crisis and escalating environmental concerns caused by climate change, which are attributed to the over-consumption of energy, have brought forth a multitude of puzzles that necessitate attention. To effectively tackle these issues, it is imperative to focus on developing efficient technologies for carbon utilization and recycling (Stolarczyk et al., 2018; Cai et al., 2021; Li et al., 2022). Photocatalysts, which employ solar simulators to reduce CO_2 into organic matters or valuable fuels like carbon monoxide, and formic acid, have brought to the forefront from researchers. Until now, a mass of photocatalysts, have been documented for the purpose of CO_2 photo-reduction, consisting metal oxides, semiconductor materials, metal organic frameworks (MOFs), and quantum dots among others (Wang et al., 2021; Wu et al., 2023a; Wu et al., 2023b; Yu et al., 2023a). However, photocatalysts still have some drawbacks and challenges, caused by the limited light absorption range, poor stability, low catalytic activity and high compounding rate of photoelectrons and holes so on (Gong et al., 2022; Ma et al., 2023). Under these circumstances, improving and enhancing photocatalytic performance remains a major challenge, for which approaches such as the design of materials, interface engineering, and loading materials might be effective strategies.

In various domains of photocatalysis, the exceptional performance exhibited by transition metal sulfide photocatalysts can be attributed to their distinctive optical and electrical properties. Among them, $ZnIn_2S_4$ (ZIS) has a prominent layered structure, a tunable forbidden band width, environmental friendliness and simplicity in synthesis (Wu et al., 2023c). Furthermore, the two dimensional nanosheet structure of ZIS also shortens the diffusion distance of charge carriers (Dang et al., 2021). However, limited CO_2 adsorption, the fast recombination of photogenerated electron-hole pairs, and restricted migration capability prevent the utilization of ZIS in photocatalysis, which seriously constrains its photocatalytic activity (Xu et al., 2014; Yi et al., 2023). Thus, it is crucial for remarkable CO_2 photocatalysis to find a material that exhibits excellent CO_2 adsorption, tunable active sites to effectively enhance electron transfer, as well as inhibits electron-hole pair complexation by forming a tight interfacial interaction strategy by complexing with ZIS.

Fortunately, metal–organic frameworks (MOFs) are a type of porous substance characterized by a crystal structure in three dimensions (3D), comprising clusters of metal–oxygen and ligands derived from organic compounds. Highly stable UiO-66-NH_2, characterizes by large surface areas, adjustable porous dimensions, designable porous structures and outstanding gas adsorption performance, which exhibits potential as a candidate for CO_2 photoreduction. Nevertheless, the narrow range of light absorption, wide bandgap, and high recombination of electron-hole pairs generated by light hinder the efficiency of photocatalysis when using MOFs as catalysts (Chen et al., 2020; Wang et al., 2020). Several tactics can be employed to enhance the photocatalytic efficiency of MOFs, such as metal doping (Dai et al., 2022) addition of co-catalysts

---

* Corresponding author.

https://doi.org/10.1016/j.arabjc.2024.105975
Received 15 May 2024; Accepted 20 August 2024

(Mahmoud et al., 2019). Moreover, One possible method to improve the photocatalytic activity is by combining light-trapping semiconductor materials with MOFs to form heterostructures, which can effectively separate photogenerated carriers, including UiO-66-NH_2@TpPa-COF (Yu et al., 2023b), CuO/Ag/UiO-66 (Zhang et al., 2022), UiO-66-NH_2/CuZnS (Sun et al., 2023).

Since the physicochemical properties of MOFs and metal sulfide can complement each other in CO_2 photocatalytic reduction, the photocatalytic performance could be improved at a large extent. During my research, the heterojunction of UiO-66-NH_2/$ZnIn_2S_4$ was constructed in-situ using the low-temperature hydrothermal method and utilized for CO_2 photoreduction. The optimized sample UiO-66-NH_2/$ZnIn_2S_4$-2 achieved a CO evolution rate of 57 μmol $g^{-1}h^{-1}$, surpassing the pure UiO-66-NH_2 and $ZnIn_2S_4$ samples by approximately 3.35 and 2.71 times, respectively. The improved catalytic property is affiliated to 1) the intimate interaction between UiO-66-NH_2 and flower-like $ZnIn_2S_4$, which accelerates the transmission of electrons and significantly promotes the separation of photogenerated carriers, 2) the large specific surface area and high CO_2 adsorption, which lay the foundation for the next catalysis. Importantly, the randomly stacked UiO-66-NH_2 on $ZnIn_2S_4$ can avoid particle aggregation. In addition, photoluminescence decay tests and transient photocurrent densities demonstrate that the composites have a strong ability to accept photogenerated electrons and maximize the reactive sites, which facilitates the directed movement of photogenerated excitons towards CO_2 reduction, thereby providing persistent electrons.

2. Results and discussion

The UiO-66-NH_2/ZIS heterojunction materials are obtained through the in-situ assembly of the pre-composited UiO-66-NH_2 octahedron onto the three-dimensional flower-like ZIS (refer to the experimental details in the Supporting Information). Fig. 1 demonstrates the morphologies obtained by the scanning electron microscopy (SEM) reflections of UiO-66-NH_2, ZIS and UiO-66-NH_2/ZIS-2. A pure ZIS sample is observed to be assembled from many nanosheets into flower-like spheres in Fig. 1a, which exhibit similar morphologies were also reported in other articles (Sun et al., 2021; Raja et al., 2023). In Fig. 1b, it can be observed that the approximate dimensions of the UiO-66-NH_2 sample is around 70 nm, and the sample possesses a consistent and symmetrical octahedral structure with uniform shape. In Fig. 1c, for the UiO-66-NH_2/ZIS-2 composite, a flowery spherical shape was primarily investigated, and the nanoparticles allocated to UiO-66-NH_2 could be discovered in the sandwich-like structure of the flower-like spherical ZIS. Fig. S1 further demonstrates the morphologies of UiO-66-NH_2, ZIS, and UiO-66-NH_2/ZIS-2 from different angles.

Fig. 1d and e show the specific marginal morphologies of UiO-66-NH_2/ZIS-2 at the nanoscale, as observed through transmission electron microscopy (TEM) and high-resolution TEM (HR-TEM). The heterojunction UiO-66-NH_2/ZIS-2 exhibited a villiform margin consisting of flower-like spherical ZIS, whereas UiO-66-NH_2 nanoparticles were found on the villiform margins (Fig. 1d). In Fig. 1e, the images of UiO-66-NH_2/ZIS-2 mainly exhibit the crystal planes (1 0 2) and (1 1 0), corresponding to ZIS lattice spacings of approximately 0.320 nm and 0.197 nm, respectively. Combined with the HR-TEM image, Fig. 1f demonstrates that the UiO-66-NH_2/ZIS-2 possesses a polycrystalline structure, as evidenced by the corresponding selected area electron diffraction (SAED) pattern.

To determine the chemical composition and distribution of elements in the UiO-66-NH_2/ZIS-2 material synthesized, we conducted the energy-dispersive X-ray spectroscopy (EDX) measurement. The EDX spectrum confirms the presence of N, S, In, Zn and Zr in the material (Fig. 1g). Furthermore, the images obtained from mapping the corresponding elements indicate a homogeneous distribution of these aforementioned elements on the heterojunction UiO-66-NH_2/ZIS-2 nanoparticles.

X-ray diffraction (XRD) patterns were performed to obtain the crystal structures of UiO-66-NH_2, ZIS and UiO-66-NH_2/ZIS (Fig. 2a). The XRD pattern of UiO-66-NH_2 is consistent with the simulated diffraction peaks (Wang et al., 2020). For pure ZIS, the three peaks centered at 22.7, 27.6 and 47.20° are indexed to the (0 0 6), (1 0 2) and (1 1 0) planes according to the standard hexagonal phase (PDF#24-1445). No other peaks are detected in the pure samples, indicating successfully prepared of UiO-66-NH_2 and ZIS. For the heterojunction UiO-66-NH_2/ZIS composite, both UiO-66-NH_2 and ZIS peaks are found, with a slight increase in diffraction peak intensity as the proportion of UiO-66-NH_2 increases.

The fourier transform infrared (FT-IR) spectra was employed to evaluate alterations in the surface's functional groups of the UiO-66-

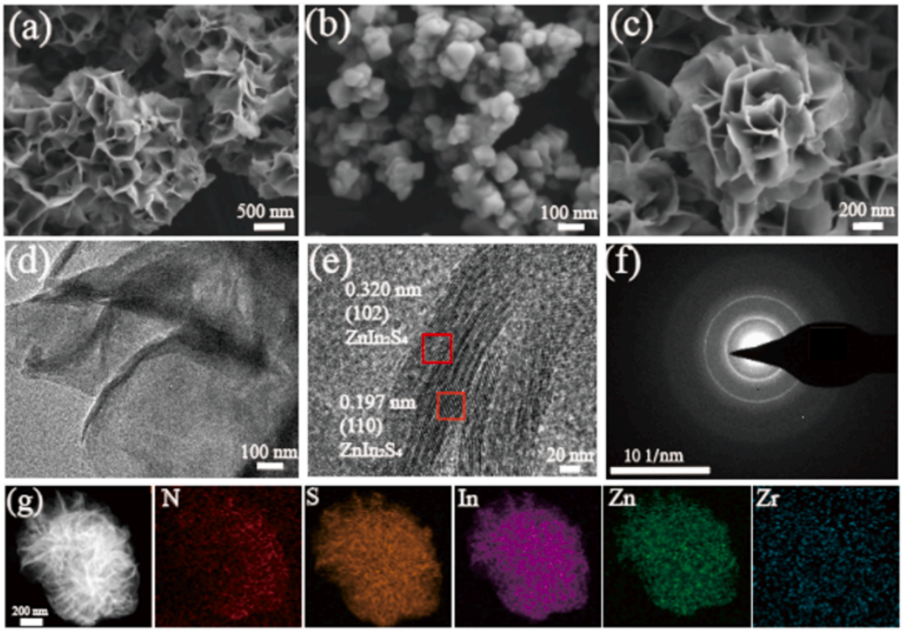

Fig. 1. SEM results of ZIS (a), UiO-66-NH_2 (b), UiO-66-NH_2/ZIS-2 (c). TEM results of (d), HR-TEM images of (e), SAED images of (f) and EDX elemental mapping of UiO-66-NH_2/ZIS-2 (g).

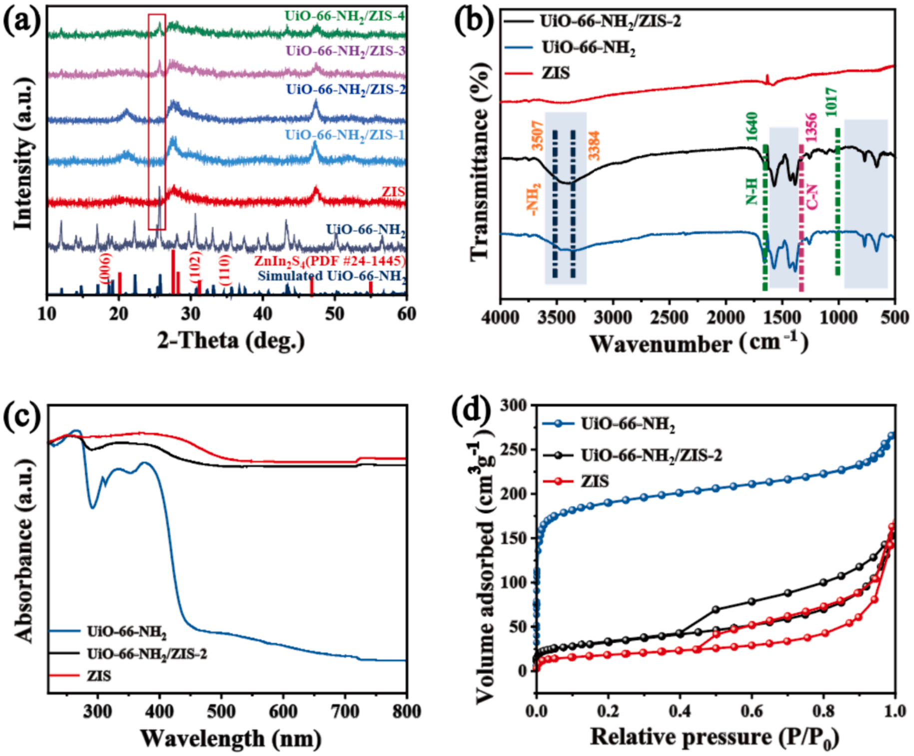

Fig. 2. (a) XRD patterns of the as-prepared UiO-66-NH_2, ZIS and UiO-66-NH_2/ZIS-y (y = 1, 2, 3, 4) samples. (b) FT-IR spectra patterns, (c) UV–Vis–NIR absorption spectra, (d) Nitrogen adsorption–desorption isotherms of UiO-66-NH_2, ZIS, and UiO-66-NH_2/ZIS-2.

NH_2/ZIS-2 heterostructure. Fig. 2b demonstrates two distinct peaks around 3507 and 3384 cm^{-1} in UiO-66-NH_2, which correspond to the asymmetric and symmetric stretching vibrations of the —NH_2 functional groups, respectively (Kandiah et al., 2010). In addition, two distinct peaks are observed at around 1640 and 1356 cm^{-1}, which correspond to the bending vibration of N—H bonds and the characteristic stretching vibration of C—N bonds in aromatic amines. However, in the FT-IR spectrum of UiO-66-NH_2/ZIS-2, the peaks at 3507, 3384 and 1640 cm^{-1} become obviously weaker compared with UiO-66-NH_2, which might be due to the interaction between —NH_2 and ZIS. A string of characteristic bands around 1600–1450 and 900–650 cm^{-1} can be imputed to benzene skeleton stretching and in-plane bending vibrations of the benzene ring respectively, demonstrating that complete MOFs structures are maintained for UiO-66-NH_2 within heterojunctions.

The optical properties of ZIS, UiO-66-NH_2, and UiO-66-NH_2/ZIS-2 were analyzed using UV–Vis–NIR diffuse reflectance spectroscopy (DRS) (Fig. 2c). Other UV diagrams of the prepared catalysts are placed in the Supporting Information (Fig. S7). The UiO-66-NH_2 exhibited the visible absorption with a slight peak at 395 nm that disappeared around 430 nm. Interestingly, ZIS and UiO-66-NH_2/ZIS-2 showed comparable consequences, which was a maximum absorption located at 445 nm with an extended tail reaching to 800 nm, suggesting that the heterojunction UiO-66-NH_2/ZIS-2 provides a solid foundation for light capture in subsequent photocatalytic reduction.

The Brunauer-Emmett-Teller (BET) specific surface area and pore size distribution of UiO-66-NH_2, ZIS and UiO-66-NH_2/ZIS-2 were analyzed using the nitrogen adsorption–desorption method (Fig. 2d). We observe ZIS presents a typical IV-type isotherm with the existence of an H3-type hysteresis loop (Wang et al., 2022). The curve of UiO-66-NH_2 shows a typical of a type I isotherm (Fu et al., 2019). The curve of the composites UiO-66-NH_2/ZIS-2 manifests itself as mixture of type I and type IV isotherms. The BET specific surface area of UiO-66-NH_2/ZIS-2 (144 m^2 g^{-1}) on Table S1 exceeded that of ZIS (63 m^2 g^{-1}), yet fell short of UiO-66-NH_2 (739 m^2 g^{-1}), thereby potentially offering more CO_2 reaction sites compared to ZIS. In this study, the BJH (Fig. S2) pore size distribution further confirms the microporous structure of UiO-66-NH_2 (Fu et al., 2019), mesoporous structure of ZIS (Peng et al., 2020), and mesoporous structure of the composite UiO-66-NH_2/ZIS-2.

It is very significant for the CO_2 capture capability of a photocatalyst. Thus, CO_2 adsorption isotherms were characterized at 298 K (Fig. S9). The isotherm measurement of UiO-66-NH_2/ZIS-2 (15 cm^3 g^{-1}) exhibits a moderate adsorption amount, which is lower than that of UiO-66-NH_2 (33 cm^3 g^{-1}) but much higher than that of ZIS (3 cm^3 g^{-1}). The results illustrate that the introduction of UiO-66-NH_2 was responsible for the enhanced CO_2 adsorption of the composite.

The X-ray photoelectron spectroscopy (XPS) was employed to analyze the surface element composition and coordination states of UiO-66-NH_2, ZIS and UiO-66-NH_2/ZIS-2. XPS survey spectra indicate that Zr, N, Zn, S, and In elements can be detected in the heterojunction UiO-66-NH_2/ZIS-2, which are in according with the EDX results (Fig. 3a). The peaks of N 1s in UiO-66-NH_2 can be fitted to two peaks at 399.50 eV and 401.70 eV, which are involved in the formation of amino groups and N—C bonds, respectively (Fig. 3b) (Fang et al., 2024). However, N 1s spectra of UiO-66-NH_2/ZIS-2 shift to 398.55 and 400.75 eV, respectively, which reveal that the coordination state of N changes obviously, possibly due to the interaction between UiO-66-NH_2 and ZIS. While for Zn, the peaks at 1022.73 and 1046.03 eV are corresponding to $2p_{3/2}$ and $2p_{1/2}$ orbitals, respectively (Fig. 3c), demonstrating the presence of the Zn^{2+} state (Liu et al., 2018). Fig. 3d depicts the In 3d spectra in UiO-66-NH_2/ZIS-2, where In $3d_{5/2}$ and In $3d_{3/2}$ correlate with 445.33 and 452.88 eV, respectively, thus suggesting that its valence state is +3 (Wang et al., 2018). Besides, Fig. S3a and b present the XPS results for Zr and S, respectively (Wang et al., 2023a; Nie et al., 2023). Changes in electron density can be analyzed by the elemental binding energies (Wang et al., 2019). As the above mentioned results, the binding energy of N 1s in UiO-66-NH_2/ZIS-2 shifts to the lower binding energy compared to that of UiO-66-NH_2, which implies that UiO-66-NH_2 gains electrons. Similarly, the binding energies of S 2p, In 3d and Zn 2p in UiO-66-NH_2/ZIS-2 shift towards the higher binding energies compared to ZIS, indicating a decrease in the electron cloud density of ZIS. The

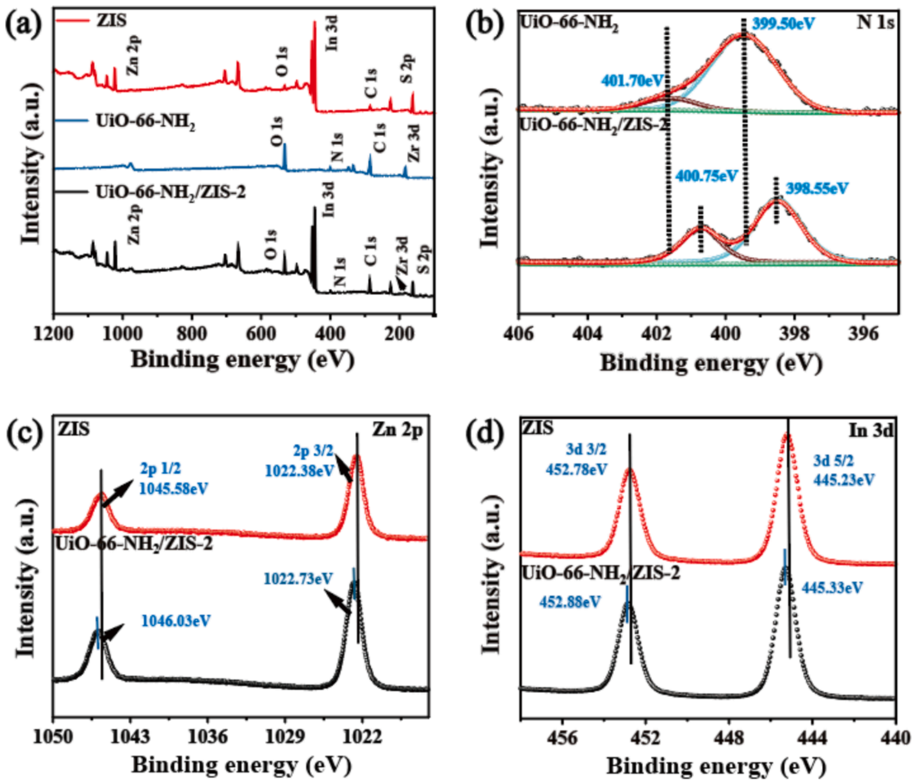

Fig. 3. XPS spectra of (a) Survey; (b) N 1s; (c) Zn 2p (d) In 3d of pure UiO-66-NH$_2$, pure ZIS, and UiO-66-NH$_2$/ZIS-2.

binding energy deviation shows that the electrons in ZIS move toward UiO-66-NH$_2$ until the Fermi energy level reaches equilibrium.

The photocatalytic CO$_2$ reduction reactions are detected using triethanolamine (TEOA) as a hole scavenger and [Ru(bipyridyl)$_3$]Cl$_2$·6H$_2$O as a photosensitizer under visible light irradiation. In Fig. 4a, the UiO-66-NH$_2$/ZIS-2 photocatalyst achieved the optimum CO yield of 57 μmol g^{-1}h^{-1}, which is approximately 3.35 and 2.71 times higher than those of the pure UiO-66-NH$_2$ (17 μmol g^{-1}h^{-1}) and ZIS (21 μmol g^{-1}h^{-1}), respectively. The CO evolution activity of UiO-66-NH$_2$/ZIS-2 is equivalent or higher than that of the latest findings (Table S2). Such findings highlight that anchoring UiO-66-NH$_2$ on flower-like ZnIn$_2$S$_4$ forming heterostructures greatly improves the CO production efficiency. The excellent performance of UiO-66-NH$_2$/ZIS-2 can be ascribed to the heterojunction between ZIS and UiO-66-NH$_2$, which accelerated the transfer and separation of charge carriers and thus improved the photocatalytic CO$_2$ performance. However, the CO$_2$ reduction activity decreases with the continued increase in the amount of UiO-66-NH$_2$, which could be attributed to the excess UiO-66-NH$_2$ covering part of ZIS and break down the balance of their synergistic effect. The CO$_2$ reduction of the composite catalysts was further investigated through several control experiments to provide a more detailed analysis. In Fig. 4b, blanking experiments were conducted under five conditions: (1) absence of photocatalyst; (2) light and Ar atmosphere; (3) none of sacrificial agent; (4) darkness; and (5) none of photosensitizer. In all blank experiments, no CO products were diagnosed except for condition (1), confirming that reactant of CO$_2$, sacrificial agent of TEOA, light irradiation, photosensitizer of [Ru(bipyridyl)$_3$]Cl$_2$·6H$_2$O and catalyst are crucial in photocatalytic CO$_2$ experiments. In Fig. 4c, the time-dependent experiments demonstrated that UiO-66-NH$_2$(Zr)/ZIS-2 exhibited a significant CO release activity for 3 h, achieving a gross yield of 235 μmol g^{-1}. Besides, to further investigate the stability of catalyst, we performed a round robin test on the best samples and found that the catalytic activity remained high after 3 consecutive reactions (Fig. S5). XRD of UiO-66-NH$_2$/ZIS-2 is the same as the as-synthesized sample (Fig. 4d), which verifies the high structural durability of the photocatalyst.

To reveal the enhancement of the photocatalytic activity over UiO-66-NH$_2$/ZIS-2, the energy level structure is studied by results of DRS, VB-XPS and Mott-Schottky plots. The bandgap energies (E_g) of UiO-66-NH$_2$, UiO-66-NH$_2$/ZIS-2, and ZIS are calculated to be 2.89, 2.62, and 2.48, respectively (Fig. S6a). VB XPS measurements were employed to investigate the valence band edges (E_{VB}). In Fig.S6b and S6c, the E_{VB} values of UiO-66-NH$_2$ and ZIS were observed at 2.75 and 1.78 eV, respectively. The flat-band potentials of ZIS and UiO-66-NH$_2$ were investigated by the Mott-Schottky mapping characterization method and tested them at 1000, 2000, and 3000 Hz (Fig. S7). When the slope of the curve is positive, it indicates that the material belongs to the n-type semiconductor (Wang et al., 2023b). Flat-band potential values were obtained from the intersection of the tangents via the three frequency tests. The flat-band potentials of UiO-66-NH$_2$ and ZIS were −0.75 V and −0.86 V (vs. Ag/AgCl). In other words, the flat-band potentials were −0.55 V and −0.66 V (vs. NHE) for normal hydrogen electrodes, respectively. Since the potential at the edge of the conduction band of the n-type semiconductor is about 0.1eV more negative than the flat band (Liu et al., 2023). Hence, the conduction band minimum (CBM) is −0.65 V vs. NHE for UiO-66-NH$_2$ and −0.76 V vs. NHE for ZIS. Based on the values of E_{CBM} and E_g, one can derive the valence band edges (E_{VBM}) using the subsequent equation:

$$E_{\mathrm{VBM}} = E_{\mathrm{CBM}} + E_g \tag{1}$$

Accordingly, the E_{VBM} values of UiO-66-NH$_2$ and ZIS are about 2.24 and 1.72 eV, respectively. Significantly, the CB and VB edges of UiO-66-NH$_2$ are found to be lower than those of ZIS, suggesting the possibility of electron transfer from ZIS to UiO-66-NH$_2$ upon photoexcitation. More importantly, the CB values of UiO-66-NH$_2$ and ZIS exhibit greater negativity in comparison to the potential of CO$_2$/CO (−0.52 eV vs. NHE) (Wang et al., 2021). Consequently, it is thermodynamically viable to convert CO$_2$ into CO on the CB of the UiO-66-NH$_2$/ZIS-2 during the photocatalytic process. The band energy positions of UiO-66-NH$_2$ and ZIS are illustrated in Fig. 5c. The positions of both the conduction and

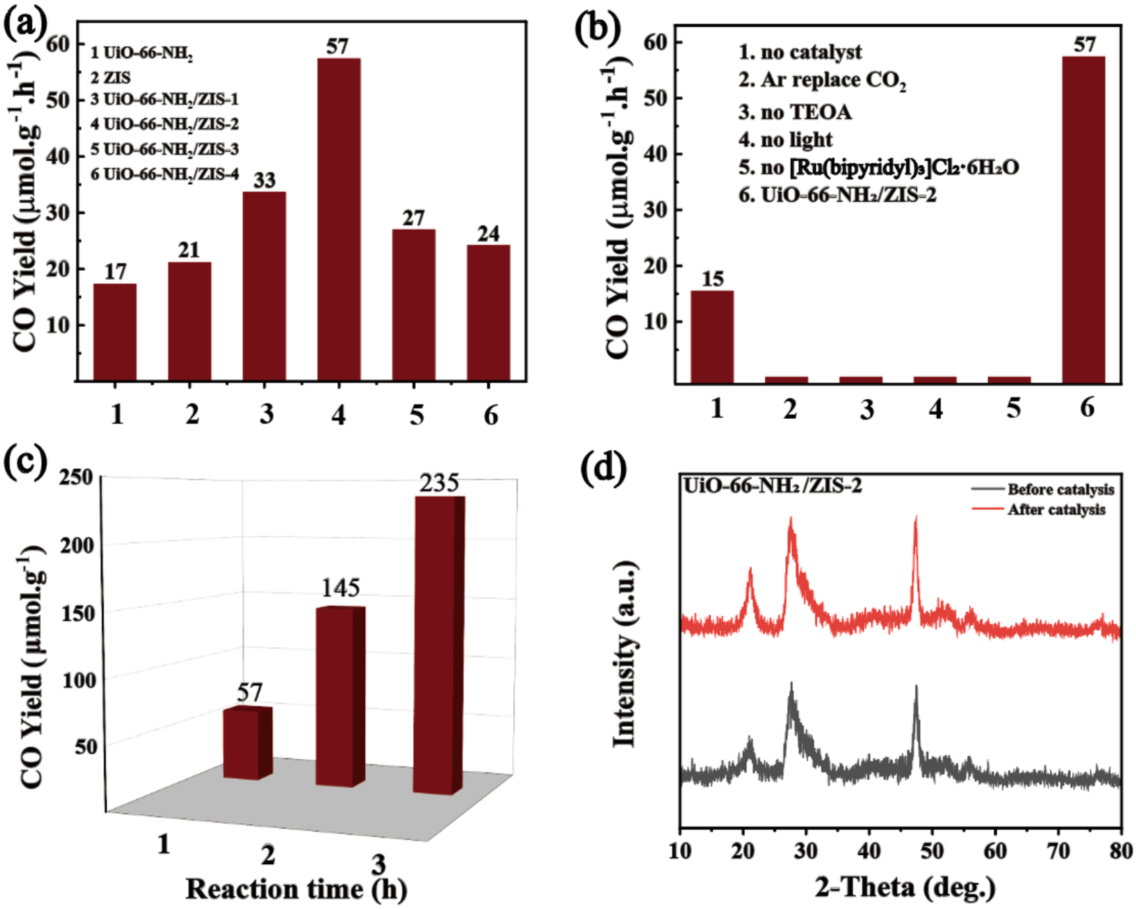

Fig. 4. (a) Photocatalytic CO_2 evolution performance of different samples. (b) The CO_2 reduction performance under various conditions. (c) CO production as a function of irradiation time. (d) X-ray powder diffraction (XRD) patterns of UiO-66-NH_2/ZIS-2 before and after CO_2 photoreduction.

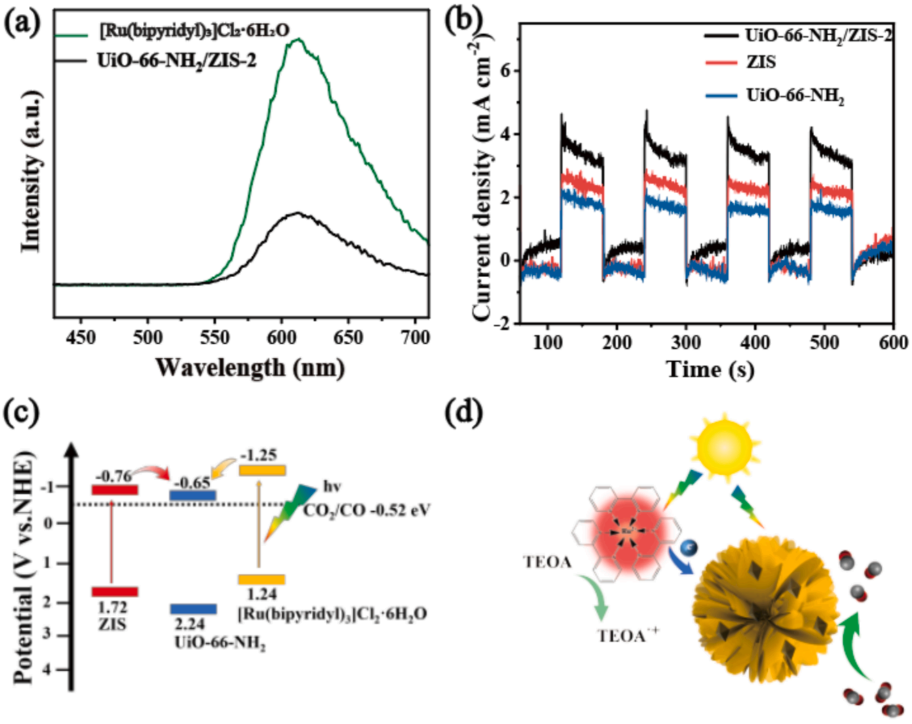

Fig. 5. Steady-state PL spectra (a) and photocurrent profiles (b) of the different samples. (c) Energy band structures of ZIS and UiO-66-NH_2. (d) Proposed mechanism of the photocatalytic CO_2 reduction over UiO-66-NH_2/ZIS-2.

valence bands of UiO-66-NH_2 are more positive than those of ZIS, leading to the formation of staggered type Z heterojunctions between them, which is in agreement with previous reports (Mei et al., 2022).

To understand the catalytic mechanism, the steady-state photoluminescence (PL) spectra display obvious PL quenching compared to photosensitizer of $[Ru(bipyridyl)_3]Cl_2 \cdot 6H_2O$ (Fig. 5a), indicating the restrained recombination of photoinduced electron-hole pairs and the efficient charge movement from $[Ru(bipyridyl)_3]Cl_2 \cdot 6H_2O$ to UiO-66-NH_2/ZIS-2 (Wang et al., 2019). To further demonstrate the carrier dynamics, the time-resolved PL spectra were examined under the similar CO_2 photocatalytic reduction system with and without catalyst of UiO-66-NH_2/ZIS-2 (Fig S10). When there is no UiO-66-NH_2/ZIS-2 in the testing system, the average lifetime of $[Ru(bipyridyl)_3]Cl_2 \cdot 6H_2O$ is 180.75 ns, which is much longer than that of system with UiO-66-NH_2/ZIS-2 (144.92 ns). The results indicate that the excited $[Ru(bipyridyl)_3]^{2+}$ is quenched by the catalyst of UiO-66-NH_2/ZIS-2, confirming the efficient electron-hole separation and transfer between $[Ru(bipyridyl)_3]Cl_2 \cdot 6H_2O$ and UiO-66-NH_2/ZIS-2. In order to investigate the efficiency of separating and transferring photogenerated carriers, the transient photocurrent analysis was performed. Fig. 5b illustrates the responses of ZIS, UiO-66-NH_2, and UiO-66-NH_2/ZIS-2 under simulated sunlight and several on/off irradiation cycles, and all samples produced stable photocurrent profiles. Among all samples, UiO-66-NH_2/ZIS-2 exhibited the highest photocurrent density, which suggests that the electron-hole pairs are effectively separated and promoted charge transfer in the heterojunction UiO-66-NH_2/ZIS-2. The photoelectrochemical findings show that the suppressed recombination and enhanced transport efficiency of photoinduced electron-hole pairs in UiO-66-NH_2/ZIS-2, thus assuring the high CO-producing rate.

Based on the results of activity assessment and photoelectrochemical results, a possible mechanism for CO_2 photocatalytic reduction is proposed (Fig. 5c and d). Under visible light irradiation, the photosensitizer of $[Ru(bipyridyl)_3]Cl_2 \cdot 6H_2O$ is excited from its valence band to conduction band. The photoinduced electrons transfer from $[Ru(bipyridyl)_3]Cl_2 \cdot 6H_2O$ to UiO-66-NH_2/ZIS-2 for CO_2 photoreduction, while the holes are consumed by TEOA to complete the entire cycle. In addition, due to the excellent visible-light absorption of UiO-66-NH_2/ZIS-2, it might produce photogenerated carriers that can be directly utilized for CO_2 photocatalytic reduction.

3. Conclusion

In summary, $ZnIn_2S_4$/UiO-66-NH_2 photocatalysts were efficiently synthesized by a facile hydrothermal method in different ratios, and it was found that the best performance of the composite photocatalyst was optimal when 10 mg of UiO-66-NH_2 was coupled with ZIS. In my research, the best composite photocatalyst was UiO-66-NH_2/ZIS-2, which demonstrated a significantly enhanced photocatalytic activity of 57 μmol $g^{-1}h^{-1}$, surpassing that of pure UiO-66-NH_2 and ZIS samples by approximately 3.35 and 2.71 times respectively. The experimental results demonstrate that this rational design not only effectively accelerates the speed of electron transmission and effectively suppress the quenching of photogenerated carriers, but also provides the large specific surface area and high CO_2 adsorption for catalytic reaction. This study provides vital knowledge for the rational design of composite structures for the highly efficient CO_2 photocatalysis into solar fuels.

CRediT authorship contribution statement

Huimin Yu: Writing – original draft, Data curation. **Shaohong Guo:** Writing – review & editing, Project administration. **Meilin Jia:** Supervision. **Jingchun Jia:** Formal analysis. **Ying Chang:** Validation. **Jiang Wang:** Validation.

Declaration of competing interest

The authors declare that they have no known competing financial interests or personal relationships that could have appeared to influence the work reported in this paper.

Acknowledgements

This work was financially supported by the Natural Science Foundation of Inner Mongolia of China (2021BS02019), the Fundamental Research Funds for the Inner Mongolia Normal University (2023JBQN045), and the National Natural Science Foundation of China (22262026).

Appendix A. Supplementary data

Supplementary data to this article can be found online at https://doi.org/10.1016/j.arabjc.2024.105975.

References

Cai, M.J., Wu, Z.Y., Li, Z., Wang, L., Sun, W., Tountas, A.A., Li, C., Wang, S.H., Feng, K., Xu, A.B., Tang, S., Tavasoli, A., Peng, M., Liu, W., Helmy, A.S., He, L., Ozin, G.A., Zhang, X.H., 2021. Greenhouse-inspired supra-photothermal CO_2 catalysis. Nat. Energy 6, 807–814. https://www.nature.com/articles/s41560-021-00867-w.

Chen, Q., Li, J., Cheng, L., Liu, H., 2020. Construction of $CdLa_2S_4$/MIL-88A(Fe) heterojunctions for enhanced photocatalytic H_2-evolution activity via a direct Z-scheme electron transfer. Chem. Eng. J. 379, 122389 https://doi.org/10.1016/j.cej.2019.122389.

Dai, S., Kajiwara, T., Ikeda, M., Romero-Muñiz, I., Patriarche, G., Platero-Prats, A.E., Vimont, A., Daturi, M., Tissot, A., Xu, Q., Serre, C., 2022. Ultrasmall copper nanoclusters in zirconium metal-organic frameworks for the photoreduction of CO_2. Angew. Chem. Int. Ed. 61, e202211848.

Dang, X.Y., Xie, M.S., Dai, F.F., Guo, J.N., Liu, J., Lu, X.X., 2021. The in situ construction of $ZnIn_2S_4$/$CdIn_2S_4$ 2D/3D nano hetero-structure for an enhanced visible-light-driven hydrogen production. J. Mater. Chem. A 9, 14888–14896. https://doi.org/10.1039/D1TA02052H.

Fang, R., Yang, Z.Q., Sun, J.J., Zhu, C.X., Chen, Y.L., Wang, Z.Q., Xue, C., 2024. Synergistic mediation of dual donor levels in CNS/BOCB-OV heterojunctions for enhanced photocatalytic CO_2 reduction. J. Mater. Chem. A 12, 3398–3410. https://doi.org/10.1039/D3TA07006A.

Fu, Y.H., Wu, J.Y., Du, R.F., Guo, K., Ma, R., Zhang, F.M., Zhu, W.D., Fan, M.H., 2019. Temperature modulation of defects in NH_2-UiO-66(Zr) for photocatalytic CO_2 reduction. RSC Adv. 9, 37733–37738. https://doi.org/10.1039/C9RA08097J.

Gong, E., Ali, S., Hiragond, C.B., Kim, H.S., Powar, N.S., Kim, D., Kim, H., In, S.-I., 2022. Solar fuels: research and development strategies to accelerate photocatalytic CO_2 conversion into hydrocarbon fuels. Energ. Environ. Sci. 15, 880–937. https://doi.org/10.1039/D1EE02714J.

Kandiah, M., Nilsen, M.H., Usseglio, S., Jakobsen, S., Olsbye, U., Tilset, M., Larabi, C., Quadrelli, E.A., Bonino, F., Lillerud, K.P., 2010. Synthesis and stability of tagged UiO-66 Zr-MOFs. Chem. Mater. 22, 6632–6640. https://doi.org/10.1021/cm102601v.

Li, P.F., Zhang, K.R., Wen, Z.S., Ma, Q.L., Liao, K.L., Huang, Z.L., Wang, Y., Li, J.H., Xu, P., 2022. Research progress on CO_2 capture and utilization technology. J. CO_2 Utiliz. 66, 102260 https://doi.org/10.1016/j.jcou.2022.102260.

Liu, H., Zhang, J., Ao, D., 2018. Construction of heterostructured $ZnIn_2S_4$@NH_2-MIL-125(Ti) nanocomposites for visible-light-driven H_2 production. Appl. Catal. B 221, 433–442. https://doi.org/10.1016/j.apcatb.2017.09.043.

Liu, S.J., Zhou, X.F., Yang, C.Q., Wei, C.H., Hu, Y., 2023. Cu atoms on UiO-66-NH_2/$ZnIn_2S_4$ nanosheets enhance photocatalytic performance for recovering hydrogen energy from organic wastewater treatment. Appl. Catal. B 330. https://doi.org/10.1016/j.apcatb.2023.122572.

Ma, G.S., Pan, Z.G., Liu, Y.F., Lu, Y.N., Tao, Y., 2023. Hydrothermal synthesis of MoS_2/SnS_2 photocatalysts with heterogeneous structures enhances photocatalytic activity. Materials 16 (12), 4436. https://doi.org/10.3390/ma16124436.

Mahmoud, M.E., Audi, H., Assoud, A., Ghaddar, T.H., Hmadeh, M., 2019. Metal-organic framework photocatalyst incorporating bis(4′-(4-carboxyphenyl)-terpyridine) ruthenium(II) for visible-light-driven carbon dioxide reduction. J. Am. Chem. Soc. 141, 7115–7121. https://doi.org/10.1021/jacs.9b01920.

Mei, Y.X., Yuan, N.C., Xie, Y.T., Li, Y.P., Lin, B.N., Zhou, Y.H., 2022. Facilely fabrication of the direct Z-scheme heterojunction of NH_2-UiO-66 and $CeCO_3OH$ for photocatalytic reduction of CO_2 to CO and CH_4. Appl. Surf. Sci. 597 https://doi.org/10.1016/j.apsusc.2022.153725.

Nie, Y., Bo, T.T., Zhou, W., Hu, H.L., Huang, X., Wang, H.Y., Tan, X., Liu, L.Q., Ye, J.H., Yu, T., 2023. Understanding the role of Zn vacancy induced by sulfhydryl coordination for photocatalytic CO_2 reduction on $ZnIn_2S_4$. J. Mater. Chem. A 11, 1793–1800. https://doi.org/10.1039/D2TA08336A.

Peng, X., Ye, L., Ding, Y.C., Yi, L.C., Zhang, C., Wen, Z.H., 2020. Nanohybrid photocatalysts with $ZnIn_2S_4$ nanosheets encapsulated UiO-66 octahedral nanoparticles for visible-light-driven hydrogen generation. Appl. Catal. B 260, 118152. https://doi.org/10.1016/j.apcatb.2019.118152.

Raja, A., Son, N.Y., Kang, M., 2023. Direct Z-scheme $ZnIn_2S_4$ spheres and CeO_2 nanorods decorated on reduced-graphene-oxide heterojunction photocatalysts for hydrogen evolution and photocatalytic degradation. Appl. Surf. Sci. 607, 155087 https://doi.org/10.1016/j.apsusc.2022.155087.

Stolarczyk, J.K., Bhattacharyya, S., Polavarapu, L., Feldmann, J., 2018. Challenges and prospects in solar water splitting and CO_2 reduction with inorganic and hybrid nanostructures. ACS Catal. 8, 3602–3635. https://doi.org/10.1021/acscatal.8b00791.

Sun, B., Bu, J.Q., Du, Y.C., Chen, X.Y., Li, Z.Z., Zhou, W., 2021. O, S-dual-vacancy defects mediated efficient charge separation in $ZnIn_2S_4$/Black TiO_2 heterojunction hollow spheres for boosting photocatalytic hydrogen production. ACS Appl. Mater. Interfaces 13, 37545–37552. https://doi.org/10.1021/acsami.1c10943.

Sun, J.T., Guan, Y.C., Yang, G.Z., Qiu, S.X., Shao, H.L., Wang, Y., Li, G.S., Xiao, S., 2023. S-scheme photocatalyst NH_2–UiO-66/CuZnS with enhanced photothermal-assisted CO_2 reduction performances. ACS Sustain. Chem. Eng. 11, 14827–14840. https://doi.org/10.1021/acssuschemeng.3c05228.

Wang, L., Cheng, B., Zhang, L., Yu, J.G., 2021. In situ irradiated XPS investigation on S-scheme TiO_2@$ZnIn_2S_4$ photocatalyst for efficient photocatalytic CO_2 reduction. Small 17, 2103447. https://doi.org/10.1002/smll.202103447.

Wang, S., Guan, B.Y., Lou, X.W.D., 2018. Construction of $ZnIn_2S_4$–In_2O_3 hierarchical tubular heterostructures for efficient CO_2 photoreduction. J. Am. Chem. Soc. 140, 5037–5040. https://doi.org/10.1021/jacs.8b02200.

Wang, Y.C., Liu, M.J., Wu, C.X., Gao, J.P., Li, M., Xing, Z.P., Li, Z.Z., Zhou, W., 2022. Hollow nanoboxes $Cu_{2-x}S$@$ZnIn_2S_4$ core-shell S-scheme heterojunction with broad-spectrum response and enhanced photothermal-photocatalytic performance. Small 18, 2400652. https://doi.org/10.1002/smll.202202544.

Wang, W.W., Song, S.J., Wang, P., He, M., Fang, Z., Yuan, X.L., Li, H., Li, C.Y., Wang, X., Wei, Y.C., Song, W.Y., Xu, H., Li, Z.X., 2023a. Chemical bonding of g-C_3N_4/UiO-66 (Zr/Ce) from Zr and Ce single atoms for efficient photocatalytic reduction of CO_2 under visible light. ACS Catal. 13, 4597–4610. https://doi.org/10.1021/acscatal.2c06255.

Wang, S., Wang, Y., Zhang, S.L., Zang, S.Q., Lou, X.W., 2019. Supporting ultrathin $ZnIn_2S_4$ nanosheets on Co/N-doped graphitic carbon nanocages for efficient photocatalytic H_2 generation. Adv. Mater. 31, 1970291. https://doi.org/10.1002/adma.201970291.

Wang, S.Q., Zhang, X.Y., Dao, X.Y., Cheng, X.M., Sun, W.Y., 2020. Cu_2O@Cu@UiO-66-NH_2 ternary nanocubes for photocatalytic CO_2 reduction. ACS Appl. Nano Mater. 3 (10), 10437–10445. https://doi.org/10.1021/acsanm.0c02312.

Wang, L.L., Zhao, Y.J., Zhang, B., Wu, G.G., Wu, J., Hou, W.H., 2023b. Spatial separation of redox centers for boosting cooperative photocatalytic hydrogen evolution with oxidation coupling of benzylamine over Pt@UiO-66-NH_2@$ZnIn_2S_4$. Cat. Sci. Technol. 13, 2517–2528. https://doi.org/10.1039/D3CY00089C.

Wu, Y., Chen, Q., Zhu, J., Zheng, K., Wu, M., Fan, M., Yan, W., Hu, J., Zhu, J., Pan, Y., Jiao, X., Sun, Y., Xie, Y., 2023a. Selective CO_2-to-C_2H_4 photoconversion enabled by oxygen-mediated triatomic sites in partially oxidized bimetallic sulfide. Angew. Chem. Int. Ed. 62, e202301075.

Wu, X.H., Chen, G.Q., Li, L.T., Wang, J., Wang, G.H., 2023c. $ZnIn_2S_4$-based S-scheme heterojunction photocatalyst. J. Mater. Sci. Technol. 167, 184–204. https://doi.org/10.1016/j.jmst.2023.05.046.

Wu, D.Y., Yin, H.Q., Wang, Z.S., Zhou, M.G., Yu, C.F., Wu, J., Miao, H.X., Yamamoto, T., Zhaxi, W.J., Huang, Z.T., Liu, L.Y., Huang, W., Zhong, W., Einaga, Y., Jiang, J., Zhang, Z.M., 2023b. Spin manipulation in a metal-organic layer through mechanical exfoliation for highly selective CO_2 photoreduction. Angew. Chem. Int. Ed. 62, e202301925.

Xu, B., He, P.L., Liu, H.L., Wang, P.P., Zhou, G., Wang, X., 2014. A 1D/2D helical CdS/$ZnIn_2S_4$ nano-heterostructure. Angew. Chem. Int. Ed. 53, 2339–2343. https://doi.org/10.1002/anie.201310513.

Yi, X.S., Zhang, S.Q., Shen, H., Li, B., Yang, L.X., Dai, W.L., Song, R.J., Zou, J.P., Luo, S.L., 2023. Atomic sulfur dissimilation remolding $ZnIn_2S_4$ nanosheets surface to enhance built-internal electric field for photocatalytic CO_2 conversion to syngas. Appl. Catal. B 338, 123003. https://doi.org/10.1016/j.apcatb.2023.123003.

Yu, X.M., Li, J., Du, M.H., Song, X.J., Huang, H.L., Nie, L., 2023b. Adaptive lattice-matched MOF and COF core-shell heterostructure for carbon dioxide photoreduction. Cell Reports Phys. Sci. 4, 101657 https://doi.org/10.1016/j.xcrp.2023.101657.

Yu, Y.T., Ma, T.Y., Huang, H.W., 2023a. Semiconducting quantum dots for energy conversion and storage. Adv. Funct. Mater. 33, 2213770. https://doi.org/10.1002/adfm.202213770.

Zhang, M.H., Wang, X., Qi, X.W., Guo, H.X., Liu, L., Zhao, Q., Cui, W.Q., 2022. Effect of Ag cocatalyst on highly selective photocatalytic CO_2 reduction to HCOOH over CuO/Ag/UiO-66 Z-scheme heterojunction. J. Catal. 413, 31–47. https://doi.org/10.1016/j.jcat.2022.06.014.